ESRF HIGHLIGHTS 2008

A light for science

ESRF

reflectivity and the phase inferred from the experimental data differ noticeably from the model calculation, suggesting that this simplest model is not fully correct.

We also reconstructed the depth-distribution of the tungsten density using the approach described in [1], which is based on the analysis of the angular dependence of the reflectivity measured after deposition of a 24.6 nm thick film. Two particular features can be clearly observed on the density profile: (a) the reduced density as compared to bulk tungsten in a region about 2 nm thick near the substrate and (b) the exponential decrease of tungsten concentration over a depth of about 1 nm within the Si substrate, probably caused by diffusion and implantation processes. These two features permit a complete explanation of both the reflectivity and the phase curves.

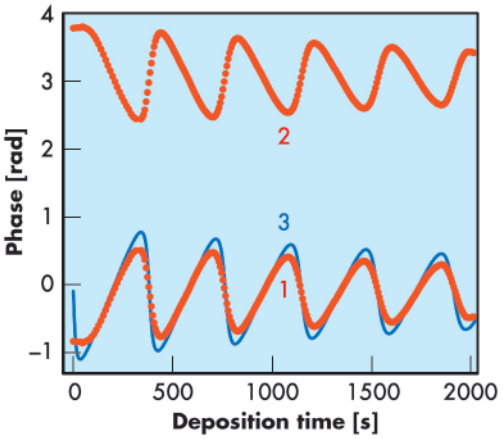

Fig. 157: Solutions of the phase retrieval problem (curves 1 and 2) found directly from the experimental curve shown in Figure 156. Curve 3 shows the phase evolution calculated assuming a uniform tungsten film with constant density. For illustrative purpose, we assumed the phase to vary within the $[-\pi / 2, 3\pi / 2]$ interval.

In the future, we plan to investigate the possibility of performing a complete angular reflectivity curve $R(\theta, t)$ instead of a single angular value at any point in time. That would allow us to find the phase versus angle, to solve the inverse problem of X-ray reflectometry more correctly, and to analyse the variations of the dielectric constant profile with time.

References

[1] I.V. Kozhevnikov, *Nucl. Instrum. Methods A* **508**, 519 (2003).

[2] L. Peverini, E. Ziegler, T. Bigault, I. Kozhevnikov, *Phys. Rev. B* **72**, 045445 (2005).

Hard X-ray interferometer based on a silicon refractive bi-lens system

Authors

A. Snigirev (a), V. Kohn (b), I. Snigireva (a), M. Grigoriev (c), S. Kuznetsov (c), V. Yunkin (c), T. Roth (a), C. Detlefs (a) and G. Vaughan (a).

(a) ESRF

(b) Kurchatov Instititute, Moscow (Russia)

(c) Institute of Microelectronics Technology, Chernogolovka (Russia)

Optical interferometers are widely used for diagnostics and metrology because of the availability of lasers with a high degree of spatial coherence. X-ray interferometry, however, has long been hampered by the lack of coherent sources. To circumvent this problem, the first X-ray interferometers used the so-called perfect crystal optics in the regime of dynamical diffraction. Due to the coherent interaction of the X-rays with a three-dimensional crystal structure, the crystal becomes an intrinsically coherent device and therefore does not require spatial coherence of the incident radiation. The classical example is the Bonse-Hart interferometer, which utilises both transmission (Laue) and surface reflection (Bragg) diffraction components.

Nowadays, the widespread availability of bright X-ray sources with sufficiently large spatial coherence, such as third-generation synchrotrons, allows researchers to observe interference by division of the wave front, similar to the classical Young's experiment. Recently a Fresnel double slit, a Fresnel double prism and a Fresnel double mirror were applied to measure the spatial coherence of synchrotron beams.

Following the successful development and application of refractive optics for high energy X-rays [1,2], we have constructed an X-ray bi-lens interferometer similar to the Billet split

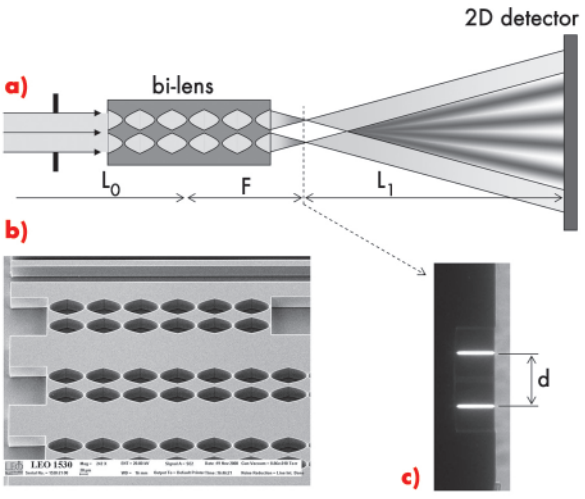

Fig. 158: **a)** Schematic drawing of the experimental set-up used for the bi-lens test. **b)** Scanning electron microscope micrograph showing a fragment of silicon bi-lenses chip. **c)** Image of the bi-lens foci recorded at a distance F = 35 mm shows the lenses split distance d = 60 µm.

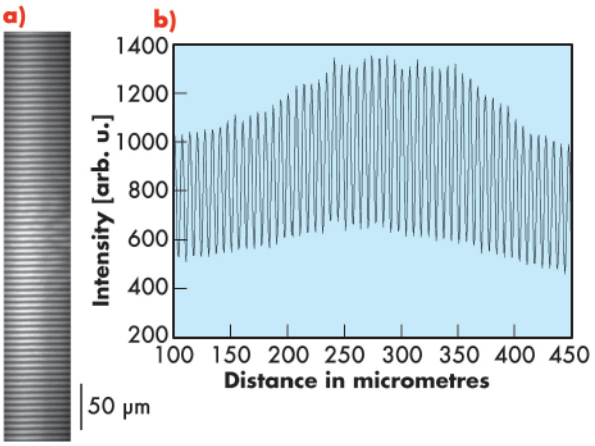

Fig. 159: **a)** Interference pattern obtained using the bi-lens interferometer of Figure 158, recorded at a distance 4 m with monochromatic beam at energy E = 12 keV. **b)** Intensity variation for a line through the centre of the fringe pattern shows a visibility (contrast) of approximately 40% corresponding to a source size S = 45 µm vertically (FWHM).

lens in classical optics. The schematic diagram of our X-ray bi-lens interferometer is shown in **Figure 158**. It consists of two identical parallel planar compound refractive lenses (CRLs) separated by a certain distance, *d*. Each lens produces an image of the source. When the lens split distance *d* is smaller than the spatial coherence length of the incoming beam, these images are diffraction limited and can be treated as coherent secondary sources. At a distance of more than twice the lens focal distance, *F*, the radiation cones diverging from these coherent secondary sources overlap, and interference occurs in the region of superposition (see **Figure 158**). Identically to the Fresnel double slit, the visibility (or contrast) of the recorded interference pattern can be used as a measure of the degree of a spatial coherence of the incident beam, or of an equivalent effective source size.

A silicon chip with a set of different linear (1D) bi-lenses was manufactured using semiconductor microfabrication technology (**Figure 158b**). The length of each single, individual lens was 100 µm and the aperture was 50 micrometres. The radius of the parabola apex was 6.25 µm. The compound refractive lenses were separated by a distance d = 60 µm.

The bi-lens interferometer was tested at beamline **ID06**. The liquid -nitrogen cooled Si-111 double crystal fixed exit monochromator (manufactured by CINEL, Italy) was used at an X-ray energy of 12 keV. The Si bi-lens chip was mounted on the microoptics test bench optics stage at a distance L_0 = 55 m from the source.

All measurements of bi-lens interference patterns were made in a vertical plane. The interference patterns were recorded by means of the high resolution X-ray CCD Sensicam camera with a spatial resolution about 1.3 µm (0.645 µm pixel size). The typical exposure time was 5-10 sec. during 16-bunch filling mode.

The observed interference pattern is shown in **Figure 159**. The fringe spacing or peak-to-peak width of the fringes is given by $\Lambda = \lambda L_1/d$, where λ is the wavelength, and L_1 is the distance from the bi-lens focus plane to detector plane. The measured spacing, Λ = 6.25 µm, is in very good agreement with calculations. The quality of the fringes produced by a bi-lens system can be described quantitatively using the visibility $V = (I_{max} - I_{min})/(I_{max} + I_{min})$, where I_{max} and I_{min} are the irradiances corresponding to the maximum and adjacent minimum in the fringe system. It is easy to show that the visibility V is directly related to the source size, S, as follows:

$$S = \frac{\Lambda L_0}{L_1}\left(-\frac{\ln V}{3.56}\right)^{1/2}$$

The measured visibility was close to 40%, corresponding to an effective source size in the vertical direction of about 45 µm (FWHM).

The bi-lens interferometer presented here has major advantages over existing methods. Manufacturing of micro-slits, mirrors and prisms for hard X-rays is a challenging technological task considering the requirements to the surface and shape (edges) quality. Whereas for silicon planar lenses, the well-developed microelectronics technology is used providing superior lens quality **[3]**. Compared to slits, mirrors and prisms, the compound refractive bi-lens system can be used at high photon energies up to 100 keV.

The applications of the bi-lenses are not limited to coherence characterisation. They can easily be extended to coherent imaging techniques. As with a classical interferometer, the bi-lens interferometer generates two coherent beams separated in space and then coherently recombines them

References
[1] A. Snigirev, V. Kohn, I. Snigireva, B. Lengeler, *Nature* **384**, 49 (1996).
[2] V. Aristov, M. Grigoriev, S. Kuznetsov, L. Shabelnikov, V. Yunkin, T. Weitkamp, C. Rau, I. Snigireva, A. Snigirev, M. Hoffmann, E. Voges, *Appl. Phys. Lett.* **77**, 4058 (2000).
[3] A. Snigirev, I. Snigireva, M. Grigoriev, V. Yunkin, M. Di Michiel, S. Kuznetsov, G. Vaughan, *SPIE* **6705**, 670506-1 (2007).

producing the interference pattern. One can easily insert a sample into one of the beams while they are separated. Any interaction with the beam would then induce significant changes in the interference pattern. From the new phase pattern, one should then be able to extract information concerning the nature and degree of interaction of the sample with the beam, leading, eventually, to a holographic reconstruction of the sample.

Capturing the shape of macromolecular crystals in 3D

Principal publications and authors

R.M.F. Leal (a,b,c), S.C.M. Teixeira (b,c), V. Rey (a), V.T. Forsyth (b,c) and E.P. Mitchell (a,c); *J. Appl. Cryst.* **41**, 729-737 (2008);
S. Brockhauser (d), M. Di Michiel (a), J.E. McGeehan (d), A.A. McCarthy (d) and R.B.G. Ravelli (d,e); *J. Appl. Cryst.* **41**, 1057-1066 (2008).

(a) ESRF
(b) ILL (France)
(c) EPSAM and ISTM, Keele University (UK)
(d) EMBL, Grenoble Outstation (France)
(e) Leiden University Medical Center (LUMC) (The Netherlands)

Absorption correction algorithms have been used for decades, in particular by crystallographers. The first approaches to reduce the effects of absorption were made by physically reshaping the sample to reach simple geometries, such as spherical or cylindrical, so that tabulated corrections could be applied easily. When the crystal could not be reshaped, Albrecht's [1] method was widely used, it relies on a precise description of the crystal geometry in order to determine the correction graphically.

However, macromolecular crystallography (MX) demanded a different approach. During MX experiments an undefined volume of cryoprotectant buffer is used to hold the macromolecular crystal within a nylon or Kapton loop prior to vitrification and data collection at cryotemperatures (100 K). Such a complex system, often with highly irregularly shaped crystals, is almost impossible to characterise manually with a description of all of the elements contributing to the absorption process, particularly the liquor surrounding the crystal. Most scaling software used in MX today employs an entirely empirical function which minimises the differences between symmetry-equivalent reflections to correct for absorption effects (as well as for the correlated crystal decay and beam effects). With the use of increasingly fragile samples having high radiation sensitivity, complete and redundant data sets may not be obtainable from a single crystal, in turn defeating the fully empirical method. Other methods are therefore needed to optimise such data sets – of particular importance where small signals are being recorded, such as anomalous data from sulphur or phosphorus atoms that commonly occur naturally in proteins or nucleic acids.

Studies on two methods to supply three-dimensional shape information recorded directly from the cryocooled crystals in vitrified buffer and supporting loop have been carried out. One uses the standard visible-light microscope systems installed on all of the ESRF MX beamlines to build a three-dimensional model based on reconstruction from shape-from-silhouettes of the crystal, buffer and loop components; the second uses X-ray microtomography to determine the three-dimensional shape of the crystal within its surrounding liquid and sample holder.

Visible light silhouettes

The key aim behind this method is to provide a routine system to build three-dimensional models of the crystal-buffer-loop system by exploiting a standard on-axis sample visualisation system that incorporates a high-quality on-axis camera system for sample alignment. As part of this

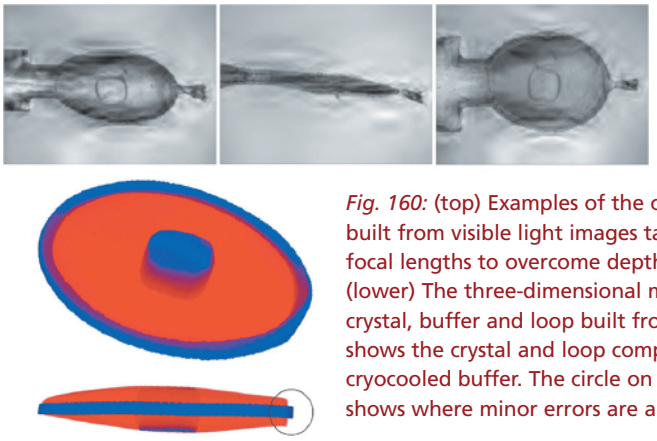

Fig. 160: (top) Examples of the composite images built from visible light images taken at different focal lengths to overcome depth-of-field issues; (lower) The three-dimensional model of the insulin crystal, buffer and loop built from the images. Blue shows the crystal and loop components, and red the cryocooled buffer. The circle on the lower image shows where minor errors are apparent in the model.

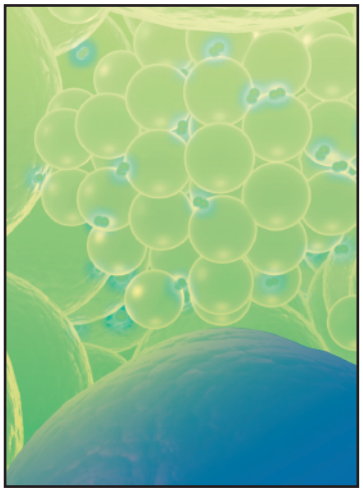

Cover image

How do palladium nanoclusters behave in hydrogen? Di Vece and co-authors observed hydrogen-induced Ostwald ripening, the growth of larger palladium nanoclusters at the expense of the smaller ones. This is a schematic impression of the palladium nanoclusters with interstitial hydrogen between the palladium atoms, which become free to move due to the interstitial hydrogen (see p24). Image courtesy M. Di Vece (K.U. Leuven) and J. Husson.

We gratefully acknowledge the help of:

C. Argoud, J. Baruchel, S. Blanchon, B. Boulanger, J-F. Bouteille, N.B. Brookes, J. Chavanne, M. Collignon, F. Comin, E. Dancer, P. Elleaume, A. Fitch, C. Habfast, L. Hardy, E. Jean-Baptiste, A. Kaprolat, M. Krisch, S. Larsen, G. Leonard, J. McCarthy, E. Mitchell, T. Narayanan, H. Reichert, M. Rodriguez Castellano, R. Rüffer, F. Sette, W.G. Stirling, C. Stuck, S. McSweeney, J. Zegenhagen, and all the users and staff who have contributed to this edition of the Highlights.

Editor
G. Admans
Layout
Pixel Project
Printing
Imprimerie du Pont de Claix

Communication Unit
ESRF
BP220 • 38043 Grenoble • France
Tel. +33 (0)4 76 88 20 56 • Fax. +33 (0)4 76 88 25 42
http://www.esrf.eu